

A surface plasmon platform for angle-resolved chiral sensing

Sotiris Droulias^{1, a)} and Lykourgos Bougas^{2, b)}

¹⁾*Institute of Electronic Structure and Laser, FORTH, 71110 Heraklion, Crete, Greece*

²⁾*Institut für Physik, Johannes Gutenberg Universität-Mainz, 55128 Mainz, Germany*

(Dated: 17 March 2022)

Chiral sensitive techniques have been used to probe the fundamental symmetries of the universe, study biomolecular structures, and even develop safe drugs. As chiral signals are inherently weak and often suppressed by large backgrounds, different techniques have been proposed to overcome the limitations of traditionally used chiral polarimetry. Here, we propose an angle-resolved chiral surface plasmon resonance (CHISPR) scheme that can detect the absolute chirality (handedness and magnitude) of a chiral sample and is sensitive to both the real and imaginary part of a chiral sample's refractive index. We present analytical results and numerical simulations of CHISPR measurements, predicting signals in the mdeg range for chiral samples of <100 nm thickness at visible wavelengths. Moreover, we present a theoretical analysis that clarifies how our far-field measurements elucidate the underlying physics. This CHISPR protocol does not require elaborate fabrication and has the advantage of being directly implementable on existing surface plasmon resonance instrumentation.

I. Introduction

Chirality is a fundamental property of life with far-reaching implications among all disciplines of science. Chiral sensitive techniques have enabled the study of fundamental symmetries of the universe¹, determination of biomolecular structures²⁻⁴, and development of safe and effective drugs^{5,6}, to name few of the most prominent applications of chiral sensing.

The polarimetric techniques of optical rotatory dispersion (ORD) and circular dichroism (CD) are among the most widely used research tools in modern science for chiral sensing⁷. However, polarimetric measurements are typically challenging as the measured signals are small and often suppressed by large backgrounds. To overcome the limitations of traditional polarimetry in chiral sensing, different techniques have been proposed in the recent years. These techniques, which aim to enhance the chiral wave-matter interaction, can in principle be arranged into two main categories, as they rely mainly on either (a) path-length enhancement or (b) chiral-field enhancement. The first type of techniques is primarily cavity-based, for which the ORD and CD signals are enhanced by the number of cavity-passes (typically about 10^3 - 10^4)⁸⁻¹¹. However, cavity-enhanced techniques become inadequate in systems with losses originating from absorption and/or scattering (e.g. chiral molecules within complex matrices, thin films, liquid and/or solid systems), because losses hinder the path-length enhancement. The chiral-field-enhancement techniques rely primarily on generating probing-electromagnetic-fields with chiral densities higher than circularly polarized plane waves¹²⁻¹⁸. Chiral and achiral nanophotonic systems, such as plasmonic/dielectric nanostructures and metamaterials, can generate contorted intense near-fields with high chiral densities around a resonance frequency of the nanosystem, thus amplifying the chiral-chiral interactions between them and a molecule, resulting in up to

10^6 enhanced response to weak molecular CD effects¹². However, in most demonstrations, elaborate fabrication is required and the employed nanosystems have their own intrinsic chiroptical response that contributes in the total CD signal and, thus, inhibits the absolute and quantitative measurement of chirality¹²⁻¹⁷.

Considering the importance of chiral sensing, it is vital to develop alternative schemes that overcome the above-mentioned limitations of path-length enhancement and/or chiral-field enhancement techniques. In this article we show that surface plasmon resonance (SPR) allows for an absolute measurement of chirality (handedness and magnitude) of a chiral system. SPR has become an important technology in the areas of biochemistry, biology, and medical sciences because of its real-time, label-free, and noninvasive nature (see Refs.^{19,20} and references therein). We demonstrate how chiral-sensitive SPR (CHISPR) is able to quantitatively detect both the real and imaginary part of the refractive index of a chiral substance (responsible for the refraction and absorption, respectively), contrary to most demonstrations that employ metallic nanostructures and/or metasurfaces. We show that CHISPR is particularly suitable for chiral sensing from thin samples which are not easily measurable using alternative techniques, and that our technique has the advantage of being applicable directly on existing SPR instrumentation without the need for additional elaborate fabrication.

In particular, using analytical calculations and numerical simulations we show how the presence of a chiral substance on top of a metal results in angular shifts in SPR measurements, with which we are able to identify the sign and quantify the magnitude of the sample's chirality. Furthermore, we demonstrate how an appropriate polarimetric analysis of the outgoing reflected beam enables the absolute measurement of signals from thin chiral layers with mdeg signals at visible wavelengths. Finally, we discuss our results using a theoretical description based on the concept of optical chirality flux²¹⁻²⁶ elucidating the underlying relation between the far-field detection scheme we employ and the near-field effects in

^{a)}Electronic mail: sdroulias@iesl.forth.gr

^{b)}Electronic mail: lybougas@uni-mainz.de

a CHISPR protocol.

II. Chiral Surface Plasmon Resonance (CHISPR)

The refractive index $n_+(n_-)$ for a right- (left-) circularly polarized (RCP/LCP) wave traversing a chiral substance is given by $n_{\pm} = n_c \pm \kappa$, where n_c is the average refractive index of the chiral substance, and κ is the substance's chirality parameter⁷. Traditional ORD and CD are typically transmission measurements, in which the rotation and absorption signals are linearly proportional to the chirality parameter κ ⁷. In particular, rotation is proportional to $\text{Re}(\kappa)$ while absorption to $\text{Im}(\kappa)$. However, if the chiral material thickness becomes comparable to the interrogation wavelength, ORD and CD signals become $< 1 \mu\text{deg}$ ^{10,11} (in the visible range; mdeg CD signals are attainable in the UV, where strong absorption lines are present⁷) and, therefore, impractical to measure (mainly due to background contributions). An alternative configuration for probing the chiral parameter is the measurement of the reflection and/or refraction from a dielectric-chiral interface^{27,28}. In such reflection-based measurements it is possible to enhance the chiral asymmetry effects near the critical angle (which scale as $\sqrt{\kappa}$, with $\kappa \ll 1$)^{10,11,29}, when the material is electrically thick and is probed from the prism side (no critical angle exists from the air side). However, for chiral material thicknesses comparable to the interrogation wavelength, reflection measurements are not possible anymore as the chiral-air interface cannot be ignored and the critical angle is now determined by the prism-air refractive index contrast. Overall, path-length enhancement techniques can allow for enhanced ORD in transmission and reflection, but for lossy systems, as is typically the case for liquid and/or solid samples, these also become inadequate (in the case of CD path-length enhancement techniques can be used, but mainly for weak molecular transitions⁹). On the other hand, techniques exploiting the enhanced intensity and the superchiral nature of near-fields close to nanophotonic structures, may result in enhanced molecular CD responses, and can be sensitive to monolayers^{12,13,17}. However, in all demonstrated cases, so far only absorption phenomena are discussed and analyzed, and it remains unclear how the real part of the chirality parameter affects the results and whether it is a parameter detectable in these experiments¹²⁻¹⁸.

To overcome the above-mentioned limitations, we present here an angle-resolved SPR measurement scheme that allows for the absolute measurement of chirality, particularly for the case of thin (sub-wavelength) samples. We consider a SPR setup in the Kretschmann configuration³⁰, where a metal layer (typically gold) is deposited on a prism surface, upon which the chiral substance is placed. A schematic of the setup is shown in Fig. 1.

Surface plasmon polariton (SPP) waves are surface electromagnetic excitations confined to and propagating along a metal-dielectric or metal-air interface. To excite the SPP wave, a TM (p)-polarized wave is required (components E_x , H_y , E_z ; Fig. 1). The incident wave must have a high tangential wavenumber k_{inc} to match the high SPP wavenumber k_{SPP} and achieve efficient power

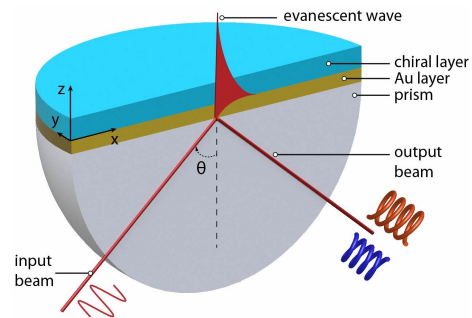


FIG. 1. A surface plasmon resonance experimental setup (Kretschmann configuration) for the detection of chirality from thin (sub-wavelength) chiral layers. A linearly TM(p) polarized beam incident on a thin gold layer (Au layer thickness ~ 50 nm) excites a surface plasmon polariton (SPP) (indicated by the evanescent wave) at a particular angle, θ , which propagates along the metal-chiral interface. The SPP wave is modified by the chiral environment, resulting in an outgoing optical chirality flux which can be used to infer the properties of the chiral layer (see text for details).

transfer to the SPP wave. In an angle-resolved experiment k_{inc} is controlled both by the angle of incidence, θ (Fig. 1), and the refractive index of the substrate (prism), n_{sub} , via $k_{\text{inc}} = k_0 \cdot n_{\text{sub}} \cdot \sin(\theta)$, where k_0 is the free-space wavenumber²⁰. As θ is scanned, maximum power transfer from the incident wave to the SPP wave is achieved at a certain angle and the excitation of the SPP wave is, therefore, manifested as a dip in an angle-resolved measured reflection. Contrary to the typical case of metal-dielectric interfaces, the presence of the chiral layer qualitatively changes the SPP wave, as was shown in Ref.³¹, generating an s-wave at the metal-chiral interface, and as such, the properties of a chiral layer should be observable through angle-resolved SPR measurements.

In Fig. 2 we present the results of a simulated angle-resolved SPR experiment in the presence of a thin chiral layer. Here, we assume operation at 633 nm, a typical wavelength for SPR instruments, and consider a prism (refractive index 1.50) coated with a 50 nm thin Au layer (Au permittivity: $-11.753 + 1.260i$ at 633 nm³²). On top of the Au layer we place a 100 nm thin layer of a chiral substance that we assume to be dispersed in water, and therefore we choose an average refractive index $n_c = 1.33$. To clarify our findings, we use a large chirality parameter κ and consider both possibilities for the sign, i.e. $\kappa = \pm 0.1$. In order to excite the SPP wave we send a p-polarized wave at angle θ , as illustrated in Fig. 1. We analyze the reflected wave in terms of s and p components and calculate the power at each polarization, namely R_s , R_p . Additionally, we analyze the total reflected power $R_s + R_p$ in terms of $+/-$ components, which we denote as $R_{\pm} = |r_{\pm}|^2$, where r_+ (r_-) is the complex amplitude of the RCP (LCP) wave (that is, $R_+ + R_- = R_s + R_p$). In an actual experiment, measurement of $R_{s/p}$ and $R_{+/-}$ can be easily performed with the incorporation of a Stokes polarimeter at the analysis stage.

In Fig. 2a we show the reflected power measured in terms of s/p waves, as is typically performed in SPR

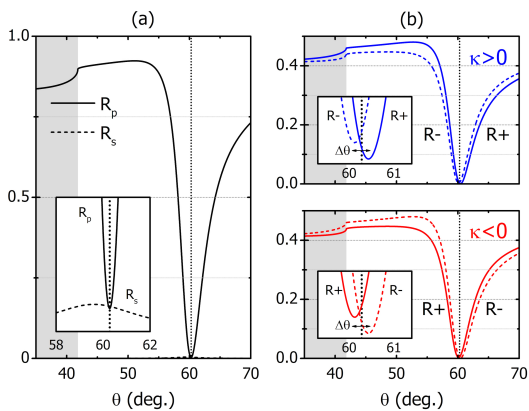


FIG. 2. SPR reflectance under the presence of a 100 nm thin chiral layer with $n_c = 1.33$. The SPR is excited with a p -wave and the reflected power is analyzed into (a) p - and s - components, R_p , R_s , respectively (same for $\kappa = \pm 0.1$), and (b) RCP(+) and LCP(-) components, R_+ , R_- , respectively (top: $\kappa = +0.1$, bottom: $\kappa = -0.1$). The effect of chirality appears in (a) as a chiral-dependent angular shift of R_p , accompanied by nonzero R_s and in (b) as a chiral-dependent angular split ($\Delta\theta = \theta_+ - \theta_-$) between R_+ and R_- . The magnitude and sign of $\Delta\theta$ depends on $|\kappa|$ and $\text{sgn}(\kappa)$, respectively. The vertical dashed lines denote the angle of minimum R_p , i.e. the SPR angle, and the shaded areas denote the region below the critical angle (41.8 deg.).

experiments. The R_p curve has a pronounced reflection-dip at 60.3 deg., indicating the excitation of a SPP wave, while we also observe a nonzero R_s peaking at 59.5 deg. (Fig. 2a, inset), as now part of the p -wave is transferred to the s -wave due to the presence of the chiral layer³¹. We emphasize here, that for $\kappa = 0$, not only $R_s = 0$ but also the R_p reflection-dip is located at 60.1 deg., that is, κ induces an angular shift on R_p . This shift is identical for both $\kappa = \pm 0.1$ and, hence, this measurement cannot differentiate between left-handed and right-handed chiral substances. However, when we analyze the reflected wave in terms of RCP/LCP (+/-) components, we observe that the minima of the R_+ , R_- reflectances do not coincide, but are separated by an angle $\Delta\theta \equiv \theta_+ - \theta_-$, where θ_+ (θ_-) denotes the angle of the R_+ (R_-) minimum (Fig. 2b). Moreover, we observe that for $\kappa > 0$ ($\kappa < 0$), $\Delta\theta > 0$ ($\Delta\theta < 0$). Thus, the presence of a thin chiral layer results in a chiral-dependent angular split $\Delta\theta$ between the measured reflectances of R_+ and R_- , which has a distinct behaviour depending on the sign and magnitude of κ .

In Fig. 3 we show the dependence of the angular split $\Delta\theta$ on the chiral substance's refractive index, n_c , and we focus on the case of real κ only (the case of imaginary κ is discussed in a following section). We observe (a) a linear dependence between the magnitudes of $\Delta\theta$ and κ (Fig.3b inset), (b) a distinct correspondence between the signs of $\Delta\theta$ and κ (Fig.3b inset), and (c) a non-monotonic dependence of $\Delta\theta$ on n_c (Fig.3b). This non-monotonic dependence is related to the interplay between the coupling strength of the incident wave to the SPP wave and the interaction strength of the SPP wave with the chiral layer. In particular, as n_c increases, the

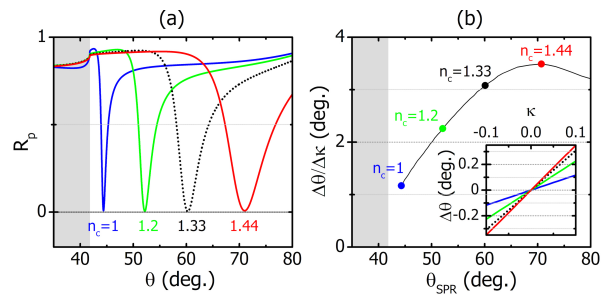


FIG. 3. Measurement sensitivity of $\Delta\theta$. (a) Angle-resolved R_p reflectance denoting the SPR angle (θ_{SPR}) for the shown selected values of n_c with $\kappa = 0$. (b) $\Delta\theta/\Delta\kappa$ vs SPR angle. The cases for n_c shown in (a) are marked with dots of the same colour. Inset: $\Delta\theta$ vs κ for the selected values of the host index n_c . The dotted line denotes the system of Fig. 2 with $n_c = 1.33$.

SPR dispersion changes and the reflection-dip is shifted to higher angles due to higher k_{SPP} (Fig. 3a). In turn, the coupling of the incident wave to the SPP becomes stronger, leading to higher $\Delta\theta$ and, hence, in increased sensitivity (Fig. 3b). Eventually, for very high incident angles the coupling of the incident wave to the SPP becomes weaker, leading to weaker $\Delta\theta/\Delta\kappa$ accordingly. For angles close to the critical angle, the effect becomes the weakest, verifying that the measurement is mediated entirely by the SPP wave and is not associated with the total-internal-reflection angle, as in the case of reflection from a dielectric-chiral interface²⁹. Thus, by measuring the magnitude and sign of this chiral-dependent angular split, we obtain absolute information about the magnitude and sign of κ .

To fully understand the mechanism behind the chiral-dependent SPR-reflectance angular split, we examine how the near-field properties of the SPP wave are associated with the properties of the reflected wave in the far-field. We start by analyzing the SPP wave along its propagation direction (x) into $+/-$ components, i.e. $\mathbf{A}_{\text{SPP}} = A_y \hat{y} + A_z \hat{z} = A_{\text{SPP}}^+ (\hat{y} + i\hat{z}) + A_{\text{SPP}}^- (\hat{y} - i\hat{z})$, where $A_{\text{SPP}}^\pm = (A_y \mp A_z)/2$ and \mathbf{A} is any of the electromagnetic field quantities \mathbf{E} , \mathbf{H} , \mathbf{B} , \mathbf{D} ; then, we calculate the electric and magnetic energy densities $w_e^\pm = (1/4)\mathbf{E}_{\text{SPP}}^\pm \cdot (\mathbf{D}_{\text{SPP}}^\pm)^*$ and $w_m^\pm = (1/4)\mathbf{B}_{\text{SPP}}^\pm \cdot (\mathbf{H}_{\text{SPP}}^\pm)^*$, respectively, which we integrate to find the total energy stored in each of the two $+/-$ components, namely $W_\pm = \int_V (w_e^\pm + w_m^\pm) d^3x$ (Fig. 4a). Here, the integration volume V is the entire SPP volume extending above the metal (where the chiral layer is to be probed). For $\kappa = 0$ we obtain $W_+ = W_-$, as the SPP wave has only an E_z -component on the yz -plane, which is equally distributed between the two $+/-$ components (typical nonchiral SPR case). This is shown in Fig. 4b, where the energy difference $W_+ - W_-$ is normalized to the incident energy $S_{\text{inc}}/2\omega$ (ω is the angular frequency and S_{inc} is the magnitude of the time-averaged Poynting vector). However, the onset of chirality causes the emergence of an E_y -component³¹ and, hence, an unbalanced storage of the optical energy between the $+/-$ components of the SPP. In fact, for $\kappa > 0$ ($\kappa < 0$), RCP (LCP) components are favoured and, therefore, $W_+ > W_-$ ($W_+ < W_-$)

(Fig. 4b). This stored energy excess between $+/-$ SPP components in the near-field results in nonzero R_s reflectance in the far-field; this is apparent in the fact that the peak of R_s coincides with the peak of $W_+ - W_-$ at 59.5 deg. which differs from the R_p minimum at 60.3 deg. (Fig. 2a and Fig. 4b). In other words, the E_y -component that emerges in the near-field due to chirality, is identified in the far-field as well, as power transfer from the outgoing p -wave to the s -wave. When the total reflected wave in the far-field is analyzed in $+/-$ components as well, the reflectance splits into two parts, which have their minima at different angles (Fig. 2b). This angular split is mediated by the resonance of the surface plasmon; the amplitude of the E_y/E_x ratio is symmetric around the SPR angle (Fig. 4c), however, the phase $\arg(E_y/E_x)$ undergoes a π -shift, favouring the advance of either the E_x or the E_y component, depending on whether the angle of incidence is below or above the SPR angle (Fig. 4c). Consequently, the mixture of the reflected RCP and LCP wave-components is weighted differently, resulting in an excess of either RCP or LCP waves below or above the SPR angle and, hence, a reflectance split between R_+ and R_- waves. As for the magnitude of κ , it does not significantly affect the $\arg(E_y/E_x)$ (it induces a slight angular shift), however, it notably changes the amplitude of E_y/E_x , which increases with increasing κ . Changing the sign of κ induces a π -shift of the E_y phase, without affecting E_x (Fig. 4c). Hence, the sign of κ does not affect the amplitude of the ratio E_y/E_x but causes the interchange between RCP/LCP components.

III. Differential measurements

We consider now measurement configurations based on differential signals which are immune to signal fluctuations and drifts. Specifically, we consider two relevant quantities associated with the reflected (outgoing) RCP/LCP waves: the amplitude and phase differential reflectance (DR), namely ρ_{DR} and ϕ_{DR} , respectively. We define the DR signals as,

$$\rho_{\text{DR}} = \frac{|r_+|^2 - |r_-|^2}{|r_+|^2 + |r_-|^2}, \text{ and } \phi_{\text{DR}} = \text{Arg} \left[\frac{r_+}{r_-} \right]. \quad (1)$$

In Fig. 5 we present the DR signals, ρ_{DR} and ϕ_{DR} , respectively, for a value of $\kappa = \pm 10^{-5}$ (which is a realistic value for the chirality parameter for, e.g., aqueous solutions of chiral molecules^{10,11}), as a function of the background index of the chiral layer, n_c . We observe ρ_{DR} signals of the order of $\sim 10^{-4}$ and ϕ_{DR} signals of the order of a few \sim mdegs, both within feasible sensitivity of SPR instruments³³⁻³⁵. As a comparison, we note that the optical rotation signal from a transmission measurement of a 100 nm chiral layer with $\kappa = +10^{-5}$ at 633 nm, is $\sim 3 \times 10^{-4}$ deg.⁷. Moreover, we observe that $\rho_{\text{DR}}(-\kappa) = -\rho_{\text{DR}}(\kappa)$ and $\phi_{\text{DR}}(-\kappa) = -\phi_{\text{DR}}(\kappa)$. Thus, with this type of measurement we are able to quantify $\text{Re}(\kappa)$ (magnitude and sign) with increased sensitivity compared to measurements of $\Delta\theta$ ^{34,36,37}.

Additionally, we observe that both differential signals, ρ_{DR} and ϕ_{DR} , decrease in amplitude as the SPR moves away from the critical angle, contrary to $\Delta\theta/\Delta\kappa$ which we observe to increase (Fig.3). This decrease is related

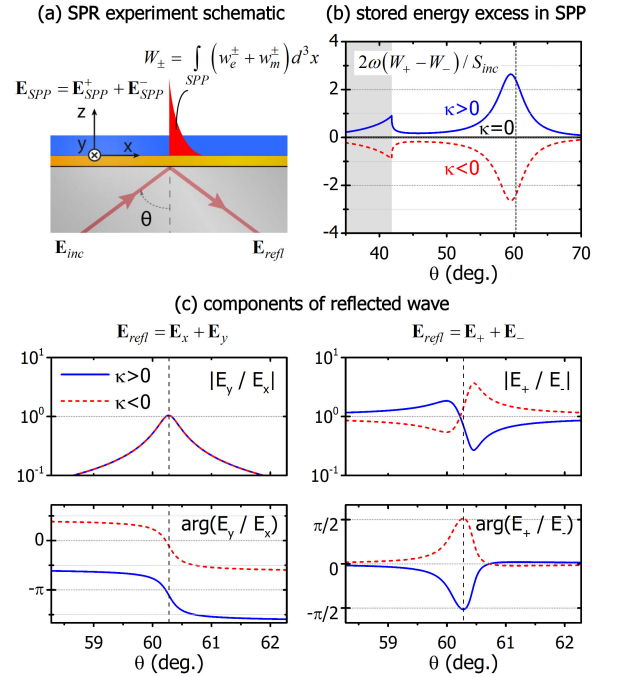


FIG. 4. Mechanism of the R_+ , R_- angular split. (a) The incident wave excites the SPP, which we analyze in RCP/LCP ($+/-$) components along its propagation direction. The total energy stored in each component is denoted as W_{\pm} (see also text for details). (b) Stored energy difference between RCP/LCP components of the SPP wave (normalized over the incident energy $S_{inc}/2\omega$). Chirality causes energy excess between RCP/LCP waves, which changes sign upon sign change of κ ($\kappa = \pm 0.1$). (c) Ratio of amplitude and phase of the reflected wave components for $\kappa = +0.1$ (solid blue lines), $\kappa = -0.1$ (dashed red lines). We analyze the wave in terms of s/p components (left) and RCP/LCP components (right). We present the amplitude in logarithmic scale to emphasize the inversion symmetry of the ratio $|E_+/E_-|$ upon sign change in κ . The vertical dashed line denotes the angle of minimum R_p , i.e. the SPR angle.

to the broadening of the SPR feature due to increased losses for higher k_{SPP} , and to the reduction of the R_s/R_p ratio, which expresses the strength of the p - to s -wave conversion. In Fig. 6 we show the change in the R_s/R_p ratio with increasing SPR angle (due to increasing n_c). We observe that the R_s/R_p ratio decreases while simultaneously broadening, which yields, thus, reduced differential signals. Moreover, the peak-to-peak values of ρ_{DR} and ϕ_{DR} ($\Delta\rho_{\text{DR}}$ and $\Delta\phi_{\text{DR}}$, respectively; Fig. 6b), qualitatively follow a similar trend indicating a strong connection with the strength of R_s/R_p . Furthermore, we observe that the variation of R_s/R_p (and consequently of $\Delta\rho_{\text{DR}}$ and $\Delta\phi_{\text{DR}}$) is non-monotonic and it generally depends on the properties of the particular metal. However, we emphasize that regardless of the exact variation, ρ_{DR} and ϕ_{DR} allow for unambiguous determination of κ .

IV. Absorption effects

In the previous sections we consider only real-valued chirality parameter κ . This is the case when one per-

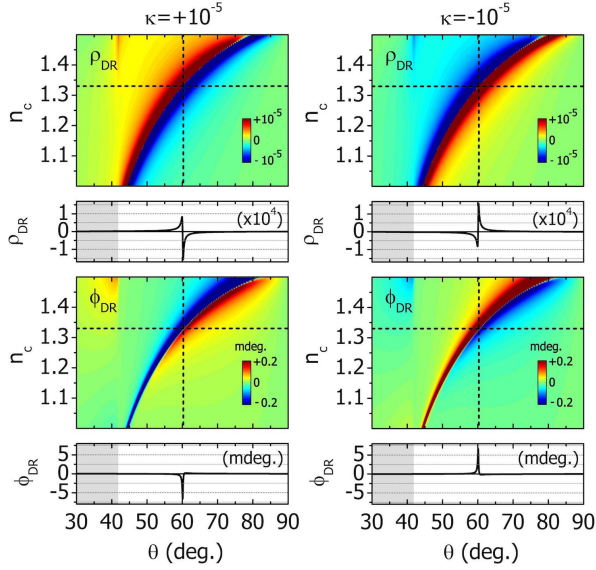


FIG. 5. Differential reflectance (DR) signals for a 100 nm thin chiral layer with $\kappa = \pm 10^{-5}$, as a function of the background index of the chiral layer (n_c). Specific examples for $n_c = 1.33$ are marked with horizontal dashed lines and are shown separately below each panel. The vertical dashed line marks the SPR angle for the chosen value of n_c .

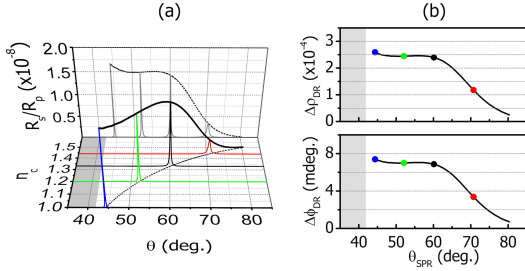


FIG. 6. Effect of coupling strength between s - and p -waves due to chirality on differential reflection measurements. (a) R_s/R_p ratio as function of n_c for $\kappa = \pm 10^{-5}$. (b) Peak-to-peak values of the differential signals ρ_{DR} and ϕ_{DR} [$\Delta\rho_{DR}$ (top) and $\Delta\phi_{DR}$ (bottom), respectively]. The marked cases in (a), (b) correspond to the cases shown in Fig. 3 using the same colour-code.

forms measurements at optical frequencies far detuned from any molecular resonances, and, as such, absorption - which is proportional to $\text{Im}(\kappa)$ - is negligible⁷. When the optical frequency of an SPR instrument is near a molecular transition, absorption becomes substantial and the proposed measurements should be interpreted with care. In order to introduce an imaginary part in the chirality parameter κ without violating the passivity we must ensure that $\text{Im}(n_c \pm \kappa) > 0$. Hence, we introduce artificial loss in the average refractive index of the chiral layer, which now is $n_c = 1.33 + 0.01i$.

In Fig. 7 we present $\Delta\theta$ as a function of $\text{Re}(\kappa)$ for $\text{Im}(\kappa) = -10^{-3}, 0, 10^{-3}$. In the presence of absorption ($\text{Im}(\kappa) \neq 0$) the angular split $\Delta\theta$ obtains a linear chiral-dependent offset, and the effects of $\text{Re}(\kappa)$ and $\text{Im}(\kappa)$ appear as linear superpositions in the total $\Delta\theta$. As an example, in Fig. 7 we use κ_0 (real variable) to control the strength of the real and imaginary part of κ and we cal-

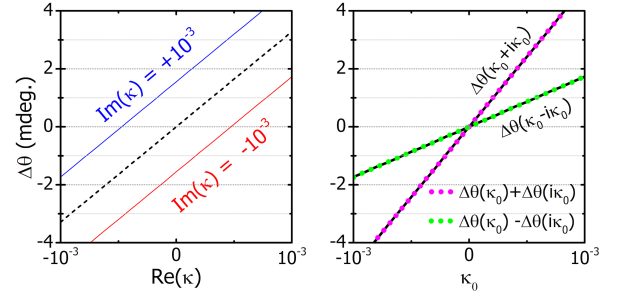


FIG. 7. Measurement sensitivity of $\Delta\theta$ in the presence of molecular absorption, i.e. $\text{Im}(\kappa) \neq 0$. (a) Scan of $\text{Re}(\kappa)$ for $\text{Im}(\kappa) = \pm 0.001i$ [dashed line corresponds to $\text{Im}(\kappa) = 0$]. (b) Demonstration of linearity of the effects of $\text{Re}(\kappa)$ and $\text{Im}(\kappa)$ on $\Delta\theta$. Here, we show $\Delta\theta$ for $\kappa = \kappa_0$ and $\kappa = i\kappa_0$ separately, and for $\kappa = \kappa_0 \pm i\kappa_0$. To maintain the passivity of the system, we add artificial loss to the chiral layer index, which now is $n_c = 1.33 + 0.01i$.

culate $\Delta\theta$ for $\kappa = \kappa_0$, $\kappa = i\kappa_0$ and $\kappa = \kappa_0 \pm i\kappa_0$. The plots of $\Delta\theta(\kappa_0 \pm i\kappa_0)$ and $\Delta\theta(\kappa_0) \pm \Delta\theta(i\kappa_0)$ are identical and, thus, verify that the effects of $\text{Re}(\kappa)$ and $\text{Im}(\kappa)$ are linearly superimposed, i.e. cumulative.

In Fig. 8 we show the change in the differential signals, ρ_{DR} and ϕ_{DR} , in the presence of absorption. Here, we again assume a κ_0 (real variable), and we calculate ρ_{DR} and ϕ_{DR} for $\kappa = \kappa_0$ and $\kappa = i\kappa_0$, and also the sum of the two signals. Additionally, we present the same quantities for $\kappa = \kappa_0 + i\kappa_0$, which we show to coincide with the sums of the individual signals (Fig. 8).

V. Optical chirality conservation

The association of the near-field features of the SPP wave with the far-field properties of the reflected wave, that we demonstrated using Poynting's theorem for conservation of energy, is closely related to another conservation law, that of optical chirality density^{21–26}. In the time-averaged, time-harmonic case this is written as,

$$-2\omega \int_V \text{Im}(\chi_e - \chi_m) d^3x + \int_V \text{Re}(\nabla \cdot \mathbf{F}) d^3x = 0, \quad (2)$$

where χ_e and χ_m are the electric and magnetic optical chirality densities, respectively, and \mathbf{F} is the corresponding chirality flux:

$$\chi_e = \frac{1}{8} [\mathbf{D}^* \cdot (\nabla \times \mathbf{E}) + \mathbf{E} \cdot (\nabla \times \mathbf{D}^*)], \quad (3)$$

$$\chi_m = \frac{1}{8} [\mathbf{H}^* \cdot (\nabla \times \mathbf{B}) + \mathbf{B} \cdot (\nabla \times \mathbf{H}^*)], \quad (4)$$

$$\mathbf{F} = \frac{1}{4} [\mathbf{E} \times (\nabla \times \mathbf{H}^*) - \mathbf{H}^* \times (\nabla \times \mathbf{E})]. \quad (5)$$

For $\kappa \neq 0$ the total chirality energy X , which is the integral of the total chirality density $\chi = \chi_e + \chi_m$ across the SPP volume, is unequally stored between the $+/-$ SPP components, i.e. $X_+ \neq X_-$, where $X_{\pm} = \int_V (\chi_e^{\pm} + \chi_m^{\pm}) d^3x$. In Fig. 9 we plot the chirality-energy excess $X_+ - X_-$ for $\kappa = 0, \pm 0.1$. The result is qualitatively similar to $W_+ - W_-$, as shown in Fig. 4b. Due to the chirality conservation law (Eq. 2), this unbalance results

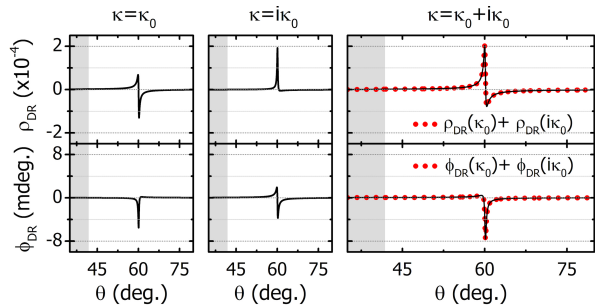


FIG. 8. Demonstration of linearity of the effects of $\text{Re}(\kappa)$ and $\text{Im}(\kappa)$ on the differential signals ρ_{DR} and ϕ_{DR} . The calculations have been performed for $\kappa = \kappa_0$ (left) and $\kappa = i\kappa_0$ (middle) separately, and for $\kappa = \kappa_0 + i\kappa_0$ (right), with $\kappa_0 = 10^{-5}$. Here we use: $n_c = 1.33 + 10^{-3}i$.

in a chirality flux \mathbf{F} in the far-field, manifested as unequal RCP and LCP components and observed through the angular split or the DR signals. In fact, as shown in Ref. ²⁶ the chirality flux \mathbf{F} of a certain propagating wave is proportional to its power flux $\mathbf{S} = \frac{1}{2}(\mathbf{E} \times \mathbf{H}^*)$ and, in particular, $F_{\pm} = \mp(\omega/c)S_{\pm}$ (where c is the vacuum speed of light, and F_{\pm} and S_{\pm} are the magnitudes of \mathbf{F} and \mathbf{S} with the signs $+/-$ corresponding to RCP/LCP waves, respectively). As a result, the reflected chirality flux F_{\pm} , normalized by the incident optical power S_{inc} , relates directly to the R_{\pm} power flux (reflectance) as $F_{\pm}/S_{\text{inc}} = \mp(\omega/c)R_{\pm}$ or $F_{\pm}/F_{\text{inc}} = R_{\pm}$, where F_{inc} is the incident chirality flux magnitude (see Supporting Information for the definition of F_{inc}). In Fig. 9 we present the fluxes F_{\pm}/F_{inc} and R_{\pm} to emphasize the equivalence between the two quantities. Therefore, we see that our proposed measurement scheme results in a direct measurement of the optical chirality flux, which is directly connected with the near-field optical chirality density ^{21–26}. Moreover, due to the linear connection between the quantities F and R , the differential reflectance amplitude ρ_{DR} is equal to the differential flux $\delta F = (F_+ - F_-)/(F_+ + F_-)$ (see Supporting Information for proof). In Fig. 9 we also demonstrate the equality between the differential flux δF and ρ_{DR} .

VI. Discussion and Conclusions

Plasmonic fields at metal-dielectric interfaces involve field-components with vanishing chirality density and chirality flow that is orthogonal to the propagation direction ³⁸. Intuitively, these properties lead to the conclusion that enhancing the optical chirality by SPPs cannot be possible. This is indeed the case when considering dielectric-metal interfaces. In contrast, at a metal-chiral interface a near-field wave is generated with non-vanishing optical chirality density and chirality flow. In this work, we demonstrate how angle-resolved CHISPR measurements allow for the detection of this near-field wave at the metal-chiral interface, resulting in absolute determination of the chirality of the chiral sample (handedness and magnitude). Moreover, in a CHISPR measurement scheme the whole evanescent-wave volume is sensitive to the probed chiral substance (due to the mobility of the propagating SPPs), contrary to schemes

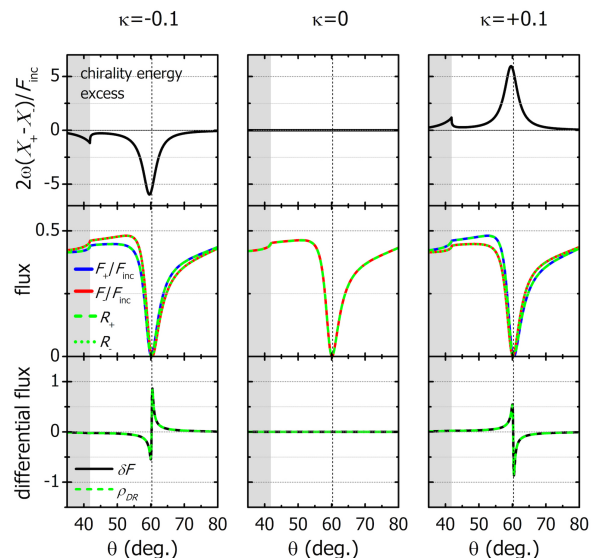


FIG. 9. Top row: Stored chirality energy difference $X_+ - X_-$ between RCP/LCP $(+/-)$ components of the SPP wave, normalized with the incident chirality energy $F_{\text{inc}}/2\omega$. Middle row: Reflected chirality flux F_{\pm} (solid blue/red lines), normalized with the incident chirality flux F_{inc} , and reflectance R_{\pm} (dashed/dotted lines). Bottom row: differential flux δF and differential reflectance amplitude ρ_{DR} . For these simulations we use a 100 nm thin chiral layer with $n_c = 1.33$ and $\kappa = -0.1$ (left column), $\kappa = 0$ (middle column) and $\kappa = +0.1$ (right column). In all panels, the SPR angle (angle of minimum R_p) is marked with a vertical dashed line.

based on local surface plasmons, where the sign and magnitude of the chiroptical response possess a complex dependence on sample geometry ^{12–17,39}. We demonstrate how a CHISPR scheme is particularly suitable for chiral sensing of thin (sub-wavelength) chiral samples, which are difficult to measure using traditional polarimetric techniques. Furthermore, the CHISPR signals we present are within the sensitivity of current SPR instrumentation for realistic values of the chirality parameter. However, the observed relationships between κ and the measured quantities ($\Delta\theta$, ρ_{DR} and ϕ_{DR}) impose a lower limit of chiral detection. This can be improved by enhancing the local fields, for example via modification of the thin metal layer, e.g. via perforation, in order to take advantage of the strong evanescent fields at the gaps. In future works we will investigate how alternative plasmonic structures can enable enhanced CHISPR detection signals.

In conclusion, we show a surface plasmon-aided scheme for probing thin (sub-wavelength) chiral films. Our proposed setup allows for combined measurements to unambiguously identify the sign and magnitude of both real and imaginary parts of the chirality parameter κ . These findings can be of great interest in chiral-biosensing applications, considering that an angle-resolved CHISPR sensing scheme is a surface-sensitive measurement and differs from conventional chiral-sensing techniques based on transmission measurements. In addition, among the advantages of our scheme are the simplicity of the setup and measurements, as it can be implemented with slight modifications of existing SPR measurement instruments, and

has also the potential for miniaturization and portable design⁴⁰. Such a possibility could enable compact devices for real-time sensing of biological processes that occur in limited regions of space.

Acknowledgements

The authors thank E. Bernikola, and A. Palmer for their feedback during the completion of this work. In addition, LB thanks G. Iwata and M. Williams for fruitful discussions. This research was supported by European Commission Horizon 2020 (grant no. FETOPEN-737071), ULTRACHIRAL Project.

- ¹E. N. Fortson and L. L. Lewis, *Phys. Rep.* **113**(5), 289 (1984).
- ²G. D. Fasman, *Circular Dichroism and the Conformational Analysis of Biomolecules* (Springer US, 2010).
- ³S. M. Kelly, T. J. Jess, and N. C. Price, *Biochim. Biophys. Acta* **1751**, 119 (2005).
- ⁴B. Nordén, A. Rodger, and T. Dafforn, *Linear Dichroism and Circular Dichroism* (The Royal Society of Chemistry, 2010).
- ⁵A. J. Hutt and S. C. Tan, *Drugs* **52**, 1 (1996).
- ⁶L. A. Nguyen, H. He, and C. Pham-Huy, *International journal of biomedical science : IJBS* **2**, 85 (2006).
- ⁷L. D. Barron, *Molecular Light Scattering and Optical Activity*, 2nd ed. (Cambridge University Press, 2004).
- ⁸J. Poirson, M. Vallet, F. Bretenaker, A. Le Floch, and J.-Y. Thépot, *Analytical Chemistry* **70**, 4636 (1998).
- ⁹T. Müller, K. B. Wiberg, and P. H. Vaccaro, *The Journal of Physical Chemistry A* **104**, 5959 (2000).
- ¹⁰D. Sofikitis, L. Bougas, G. E. Katsoprinakis, A. K. Spiliotis, B. Loppinet, and T. P. Rakitzis, *Nature* **514**, 76 (2014).
- ¹¹L. Bougas, D. Sofikitis, G. E. Katsoprinakis, A. K. Spiliotis, P. Tzallas, B. Loppinet, and T. P. Rakitzis, *The Journal of Chemical Physics* **143**, 104202 (2015).
- ¹²E. Hendry, T. Carpy, J. Johnston, M. Popland, R. V. Mikhaylovskiy, A. J. Laphorn, S. M. Kelly, L. D. Barron, N. Gadegaard, and M. Kadodwala, *Nature Nanotechnology* **5**, 783 (2010).
- ¹³Y. Tang and A. E. Cohen, *Science* **332**, 333 (2011).
- ¹⁴T. J. Davis and E. Hendry, *Phys. Rev. B* **87**, 085405 (2013).
- ¹⁵A. S. Karimullah, C. Jack, R. Tullius, V. M. Rotello, G. Cooke, N. Gadegaard, L. D. Barron, and M. Kadodwala, *Advanced Materials* **27**, 5610 (2015).
- ¹⁶Y. Luo, C. Chi, M. Jiang, R. Li, S. Zu, Y. Li, and Z. Fang, *Advanced Optical Materials* **5**, 1700040 (2017).
- ¹⁷Y. Zhao, A. N. Askarpour, L. Sun, J. Shi, X. Li, and A. Alù, *Nature Communications* **8**, 14180 (2017).
- ¹⁸E. Mohammadi, K. L. Tsakmakidis, A. N. Askarpour, P. Dehkoda, A. Tavakoli, and H. Altug, *ACS Photonics* **5**, 2669 (2018).
- ¹⁹H. H. Nguyen, J. Park, S. Kang, and M. Kim, *Sensors* **15**, 10481 (2015).
- ²⁰R. B. M. Schasfoort, ed., *Handbook of Surface Plasmon Resonance* (The Royal Society of Chemistry, 2017).
- ²¹D. M. Lipkin, *Journal of Mathematical Physics* **5**, 696 (1964).
- ²²Y. Tang and A. E. Cohen, *Phys. Rev. Lett.* **104**, 163901 (2010).
- ²³K. Y. Bliokh and F. Nori, *Phys. Rev. A* **83**, 021803 (2011).
- ²⁴M. M. Coles and D. L. Andrews, *Phys. Rev. A* **85**, 063810 (2012).
- ²⁵T. G. Philbin, *Phys. Rev. A* **87**, 043843 (2013).
- ²⁶L. V. Poulikakos, P. Gutsche, K. M. McPeak, S. Burger, J. Niegemann, C. Hafner, and D. J. Norris, *ACS Photonics* **3**, 1619 (2016).
- ²⁷M. P. Silverman, J. Badoz, and B. Briat, *Opt. Lett.* **17**, 886 (1992).
- ²⁸A. Ghosh and P. Fischer, *Phys. Rev. Lett.* **97**, 173002 (2006).
- ²⁹M. Silverman and J. Badoz, *Optics Communications* **74**, 129 (1989).
- ³⁰E. Kretschmann, *Optics Communications* **6**, 185 (1972).
- ³¹G. Mi and V. Van, *Opt. Lett.* **39**, 2028 (2014).
- ³²P. B. Johnson and R. W. Christy, *Phys. Rev. B* **6**, 4370 (1972).
- ³³M. Piliarik and J. Homola, *Opt. Express* **17**, 16505 (2009).

- ³⁴X. Wang, M. Jefferson, P. C. D. Hobbs, W. P. Risk, B. E. Feller, R. D. Miller, and A. Knoesen, *Opt. Express* **19**, 107 (2011).
- ³⁵R. C. Pooser and B. Lawrie, *ACS Photonics* **3**, 8 (2016).
- ³⁶A. V. Kabashin, S. Patskovsky, and A. N. Grigorenko, *Opt. Express* **17**, 21191 (2009).
- ³⁷S. Patskovsky, M. Meunier, P. N. Prasad, and A. V. Kabashin, *Opt. Express* **18**, 14353 (2010).
- ³⁸K. Y. Bliokh and F. Nori, *Phys. Rev. A* **85**, 061801 (2012).
- ³⁹Y. Tang, L. Sun, and A. E. Cohen, *Applied Physics Letters* **102**, 043103 (2013).
- ⁴⁰Y. Liu, Q. Liu, S. Chen, F. Cheng, H. Wang, and W. Peng, *Scientific Reports* **5**, 12864 (2015).
- ⁴¹Condon, E. *U. Rev. Mod. Phys.* **1937**, 9, 432.
- ⁴²Schasfoort, R. B. M., Ed. *Handbook of Surface Plasmon Resonance*; The Royal Society of Chemistry, 2017.

Appendix

A1. Theoretical calculations

To analytically study our proposed system, we solve Maxwell's equations $\nabla \times \mathbf{E} = i\omega\mathbf{B}$ and $\nabla \times \mathbf{H} = -i\omega\mathbf{D}$ with the appropriate boundary conditions for a chiral layer placed on top of a metal layer, both of which have finite width along the z -direction and are infinite on the xy -plane (Figure 1 of the main text). The constitutive relations in the chiral layer region are formulated according to Condon's convention⁴¹ as: $\mathbf{D} = \epsilon\epsilon_0\mathbf{E} + i(\kappa/c)\mathbf{H}$ and $\mathbf{B} = \mu\mu_0\mathbf{H} - i(\kappa/c)\mathbf{E}$, where ϵ , μ refer to the relative permittivity and permeability ($n_c = \sqrt{\epsilon\mu}$), respectively, κ is the chirality parameter, and c the vacuum speed of light. By applying the boundary conditions at each of the three interfaces, the tangential E - and H - components (E_x , E_y , H_x , H_y) form a 12×12 linear system of equations, which is then solved analytically. To verify our analytical findings we also solve the same problem numerically with full-wave vectorial Finite Element Method (FEM) simulations, utilizing the commercial software COMSOL Multiphysics. The constitutive relations are modified to include the chirality parameter κ and the computational space is terminated by Perfectly Matched Layer (PML) sufficiently far from the metal-chiral system.

A2. Optical flux, chiral flux, and reflectances

Analyzing the incident wave in $+/-$ components we calculate the magnitudes of the power flux S_{inc}^{\pm} and chiral flux F_{inc}^{\pm} for each component. Because the incident wave is linearly polarized (p-wave), we find that these quantities are equally distributed between the $+/-$ components, i.e. $S_{\text{inc}}^+ = S_{\text{inc}}^- \equiv S_{\text{inc}}/2$ and $F_{\text{inc}}^+ = F_{\text{inc}}^- \equiv F_{\text{inc}}/2$, where S_{inc} and F_{inc} are the magnitudes of the total incident power and chiral flux, respectively. In fact, because the incident wave is linearly polarized, the total chirality flux is zero, i.e. $\mathbf{F}_{\text{inc}} = \mathbf{F}_{\text{inc}}^+ + \mathbf{F}_{\text{inc}}^- = 0$. However, because the individual fluxes have nonzero magnitude (and equal; they correspond to circularly polarized waves of equal amplitude), we define the incident flux magnitude as $F_{\text{inc}} = |\mathbf{F}_{\text{inc}}^+| + |\mathbf{F}_{\text{inc}}^-| = 2|\mathbf{F}_{\text{inc}}^{\pm}| \equiv 2F_{\text{inc}}^{\pm}$.

Next, we can associate the quantities related to the incident and reflected $+/-$ components as,

$$F_{\text{inc}}^{\pm} = \mp \frac{\omega}{c} S_{\text{inc}}^{\pm}, \quad F_{\text{refl}}^{\pm} = \mp \frac{\omega}{c} S_{\text{refl}}^{\pm}, \quad (6)$$

and hence

$$\frac{F_{\text{refl}}^{\pm}}{F_{\text{inc}}^{\pm}} = \frac{S_{\text{refl}}^{\pm}}{S_{\text{inc}}^{\pm}} \Rightarrow \frac{F_{\text{refl}}^{\pm}}{F_{\text{inc}}^{\pm}} = \frac{S_{\text{refl}}^{\pm}}{S_{\text{inc}}^{\pm}} \equiv R_{\pm}, \quad (7)$$

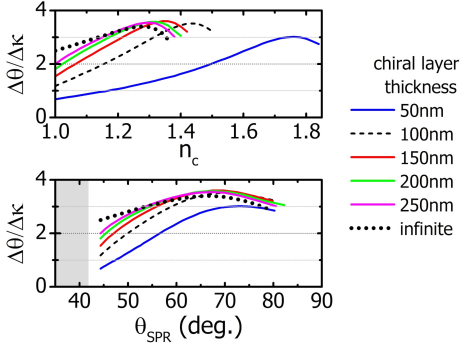


FIG. A1. $\Delta\theta/\Delta\kappa$ as a function of the chiral-layer thickness. The dashed line corresponds to the results shown in Fig. 3b of the main text (reproduced here for easier comparison), and the dotted line denotes the limit for infinite chiral layer. The results are shown up to approximately 80 deg. where the SPR dip is relatively pronounced.

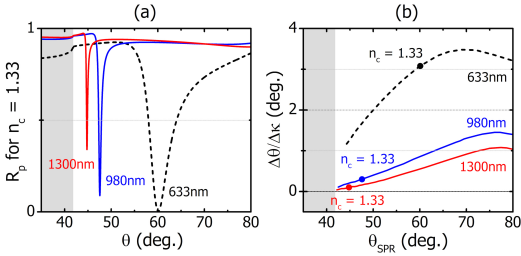


FIG. A2. Measurement sensitivity of $\Delta\theta$ of a 100 nm chiral layer and 50 nm Au layer for operation at 633 nm (black dashed lines), 980 nm (blue solid lines) and 1300 nm (red solid lines). (a) R_p reflectance for $n_c = 1.33$ and $\kappa = 0$. (b) $\Delta\theta/\Delta\kappa$ vs SPR angle. The cases for $n_c = 1.33$ shown in (a) are marked with dots of the same colour. The dashed black lines correspond to the results shown in Fig. 3b of the main text.

or simply $F_{\pm}/F_{\text{inc}} = R_{\pm}$ as we use in the main manuscript (see Fig. 9 main text).

Furthermore, using $F_{\pm}/F_{\text{inc}} = R_{\pm}$ it follows that:

$$\delta F = \frac{F_+ - F_-}{F_+ + F_-} = \frac{R_+ F_{\text{inc}} - R_- F_{\text{inc}}}{R_+ F_{\text{inc}} + R_- F_{\text{inc}}} = \frac{R_+ - R_-}{R_+ + R_-} = \rho_{\text{DR}}, \quad (8)$$

i.e. the differential chirality flux δF is equal to ρ_{DR} , as we also demonstrate in Fig. 9 of the main text.

A3. Sensitivity vs layer thickness

In Fig. A1 we repeat the calculations of the measurement sensitivity ($\Delta\theta/\Delta\kappa$) presented in Fig. 3b (main text), for chiral layers of variable thickness. We present the results in terms of n_c and the corresponding SPR angle. We see that, with increasing chiral layer thickness, the measurement sensitivity converges to the limit of chiral substances of theoretically infinite extent (practically referring to electrically thick samples). In particular, for small SPR angles this increase is monotonic, but for large SPR angles the sensitivity reaches a maximum level for a thickness of ~ 100 nm-150 nm, beyond which it gradually drops until convergence. Thus, due to the evanescent character of the SPP wave inside the chiral region, equiv-

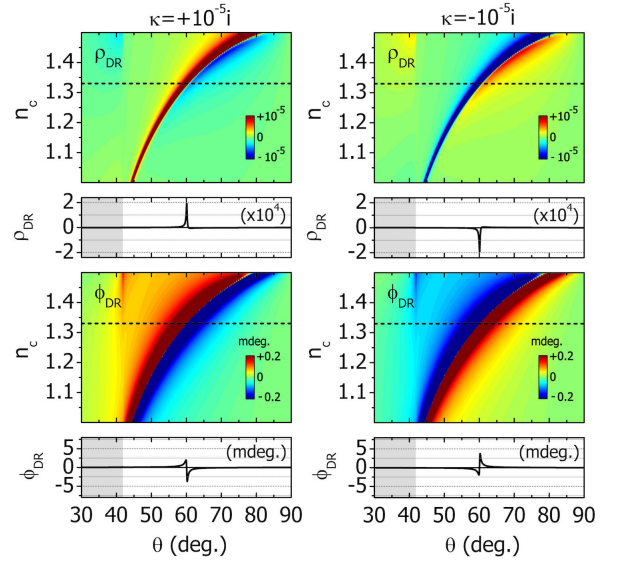


FIG. A3. Differential reflectance (DR) signals for a 100 nm thin chiral layer of purely imaginary chiral parameter $\kappa = \pm 10^{-5}i$, as function of n_c . To preserve the passivity we use $\text{Im}(n_c) = 10^{-3}i$. Specific examples for $n_c = 1.33$, are marked with a horizontal dashed line and are shown separately below each panel.

alent levels of sensitivity can be achieved for a large range of chiral-layer thicknesses.

A4. SPR measurements vs. optical wavelength

Our study, which has been focused on operation at 633 nm, provides general conclusions which are applicable to any operation wavelength that supports pronounced SPRs. However, a change of the operation wavelength will induce changes in the metal permittivity and, thus, the SPR dispersion, which may significantly change the SPR reflectance. Therefore, in order to maintain the optimum coupling of the incident wave to the SPP wave, the thickness of the metal layer must be modified accordingly.

To demonstrate the effect of the coupling strength on the measurement sensitivity, we examine the $\Delta\theta/\Delta\kappa$ dependence for three different SPR optical wavelengths (633 nm, 980 nm and 1300 nm; typical optical wavelengths used in commercial SPR instruments⁴²), without changing the metal layer thickness, which is 50 nm. As a result, the non-optimized metal thickness manifests as less pronounced SPR dips and reduced sensitivity in $\Delta\theta/\Delta\kappa$, accordingly. We show our results in Fig. A2.

A5. Differential measurements for $\text{Im}(\kappa) \neq 0$

In Fig. 8 of the main text we present differential reflectance signals for the case of purely imaginary κ , in particular for $\kappa = \pm 10^{-5}i$. These results are obtained for $n_c = 1.33 + 10^{-3}i$. For completeness, the calculations for variable $\text{Re}(n_c)$ and constant $\text{Im}(n_c) = 10^{-3}i$ are shown in Fig. A3. The peak-to-peak values of the differential reflectance signals, $\Delta\rho_{\text{DR}}$ and $\Delta\phi_{\text{DR}}$, for both purely real and pure imaginary κ are shown in Fig. A4. In both cases we consider $\text{Im}(n_c) = 10^{-3}i$. We see that the measured

signals for either purely real or purely imaginary κ are practically equal.

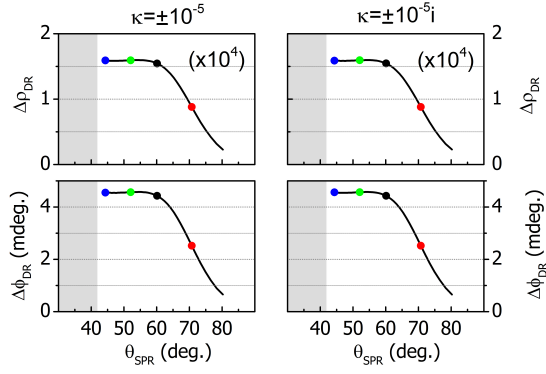


FIG. A4. Peak-to-peak values of the differential signals ρ_{DR} and ϕ_{DR} , $\Delta\rho_{DR}$ (top), and $\Delta\phi_{DR}$ (bottom) as function of the SPR angle [tuned via $\text{Re}(n_c)$], for $\kappa = \pm 10^{-5}$ (left) and $\kappa = \pm 10^{-5}i$ (right). To preserve the passivity we use $\text{Im}(n_c) = 10^{-3}i$.